University of Bristol - Explore Bristol Research

General rights
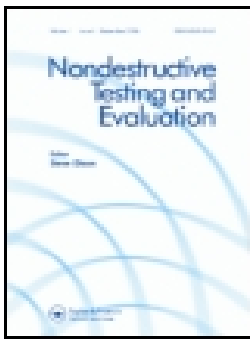
Measurement of the ultrasonic scattering matrices of near-surface defects using ultrasonic arrays

Jie Zhang, Peng Yu & Tie Gang

Taylor & Francis
Taylor & Francis Group

🔓 OPEN ACCESS

Measurement of the ultrasonic scattering matrices of near-surface defects using ultrasonic arrays

Jie Zhang[a] 🆔, Peng Yu[b] and Tie Gang[b]

[a]Department of Mechanical Engineering, University Walk, University of Bristol, Bristol, UK; [b]State Key Laboratory of Advanced Welding Production Technology, Harbin Institute of Technology, Harbin, China

ABSTRACT

Ultrasonic arrays have been widely used and developed for defect detection and characterisation over the last 10 years. In this paper, the question of how to inspect and characterise near-surface defects that are small with respect to wavelength is addressed. The challenge is to overcome the effect of the proximity of these scattered signals to high-amplitude signals reflected from structural features, such as planar surfaces. Here, a method is proposed to extract the scattered signals from a near-surface defect which overlap with signals from a structural feature in both the time and frequency domains. The extracted signals are then used to generate a scattering coefficient matrix, from which it is possible to characterise the defect. In the proposed method, the location of the defect is first approximately identified from an image. The arrival time difference between the signals from the defect and the nearby planar surfaces for each combination of transmitter and receiver array elements is then calculated. In some cases, the scattered signals can be directly separated in time from the structural features, and in other cases, they are extracted by subtracting the data with reference signals obtained in the absence of a defect. Finally, the proposed method is used to experimentally detect and characterise three different near-surface defects by extracting their corresponding scattering matrices.

1. Introduction

Fatigue cracks and stress corrosion cracks are common near-surface defects resulting from cyclic loading and harsh operating conditions in solid structures such as rail tracks, gears, vessels and pipelines.[1] Assessment of the size and type of these defects is essential in structural integrity analysis because these defects can lead to structural failure when they have reached a critical size.[2] In non-destructive evaluation, defects can be detected using a range of methods including surface waves [3–6] or guided waves.[7,8] Both methods can be used to detect defects which lie on the wave propagation path and the amplitude of the reflected or transmitted signals can also be used to indicate the defect size. Single-sided

---

access restrictions mean that ultrasonic bulk wave measurements are often made by placing a single transducer or array on the front wall of a structure to detect a defect on the back wall. [9–13] One of the benefits of using ultrasonic arrays to detect back-surface defects in this way is that one array transducer allows a given defect to be illuminated from a wide range of angles and captures the full matrix capture (FMC) data-set. An imaging algorithm, e.g. the total focusing method (TFM),[14] can then be used to post-process the FMC data and reconstruct an image to detect the defect. For a surface-breaking crack with a size around or greater than two wavelengths, Felice used the location difference between the crack tip image and the back wall image to accurately measure the crack size.[13] However, when the size of a surface-breaking crack is less than two wavelengths, the crack tip image is difficult to be recognised and used to size crack.[13] Another benefit of using ultrasonic arrays in defect inspection is that the measured FMC data-set contains the scattered wave information from the defect termed as the scattering coefficient matrix (S-matrix) which can be used to classify and size the embedded crack-like defects by searching the best matched shape in the S-matrix database.[15–19] Note that the shape of the S-matrix for a smooth crack is unique as a function of crack size divided by wavelength and hence can be used to classify and size the defect without measuring the actual scattering amplitude.[11,12,15–17]

However, in a typical FMC data-set, the signals scattered from a near-surface defect and those reflected from the back wall often overlap in both time and frequency domains and this makes S-matrix extraction difficult and this hence, hinders detection and sizing. In this paper, a method is developed to experimentally extract the S-matrix of a near-surface defect using ultrasonic arrays, typically for that with a size less than two wavelengths. A sample with a machined notch is used to assess the proposed method. The difference between the experimentally measured and simulated scattering matrices is also investigated.

2. Modelling scattered signals from a structure

The propagation of an ultrasonic wave and its interaction with a planar surface and a near-surface defect can be represented in the far field of the transducer element and defect using a hybrid forward scattering model,[20,21] which provides an efficient tool for array data simulation. Here, the model is introduced to simulate the ultrasonic wave transmitted from an array element, propagating in a structure, interacting with a near-surface defect and a planar back-wall surface, and received by another array element. This model is used to understand how the scattered signals from these features interact and explore how these signals can then be extracted to reveal the S-matrix of the defect.

Consider the 2D geometry shown in Figure 1, where Cartesian coordinates, (x, z), represent lateral position and depth with respect to the centre of the linear array. The figure schematically shows an array positioned above a test structure and two possible wave paths from a transmitter element at position vector **u** back to a receiver element at **v**. Note that the front wall and back wall of the structure are smooth and parallel.

2.1. Scattering coefficient matrix of a near-surface defect

The interaction between ultrasonic waves and a scatterer can be encoded by its far-field S-matrix which is defined as the far-field complex amplitude of the signals from a scatterer as a function of the incident and scattered angles.[16,20] When a plane wave of displacement
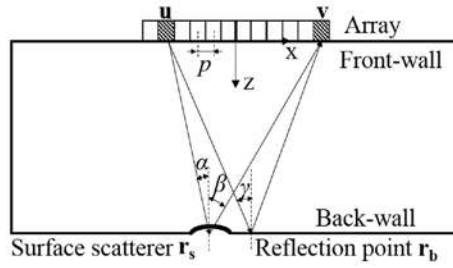
Figure 1. Schematic diagram illustrating the geometry used in the hybrid forward scattering model.

amplitude u_i is incident on a 2D scatterer, a scattered field is generated and in the far field decays in an inverse proportion to the square root of the distance from the defect. If the amplitude of the scattered wave at a distance r is u_s, then the far-field S-matrix is given by,[16,20]

$$S(\omega, \alpha, \beta) = \frac{u_s}{u_i} \sqrt{\frac{r}{\lambda}} exp(-ik(r - \lambda)), \tag{1}$$

where ω is the temporal frequency, λ is the wavelength and k is the wave number ($k = 2\pi/\lambda$). Exact analytical solutions for the S-matrix exist for a very limited number of simple shapes such as spherical or cylindrical voids [20,22] and good approximate solutions (e.g. Born or Kirchhoff [20,23]) can be applied in some cases, e.g. rough cracks. However, for near-surface defects, in general, there is no exact analytical solution, so instead computationally intensive numerical solutions are required. In this paper, a numerical method using local FE modelling without absorbing regions [12,24] was used to simulate the S-matrices from various near-surface defects. In this method, nonreflecting boundary conditions are imposed on the boundary of the modelling domain using the Green's function of an elastic half-space (see [12] for a fuller description). In this way, the size and computation cost of the model are reduced significantly. Note that the superposition of an incident plane wave and its reflections from the free surface are used as the incident field in the local FE model for calculating the S-matrix of a near-surface defect.[11] In this way, the S-matrix of the near-surface defect encodes the 'additional' scattering due to the defect. This means that all scattering, both single from the defect and multiple between the defect and the back wall are included, but the specular signals from the back wall are excluded.

2.2. Hybrid forward model to estimate scattered signal from a structure

Figure 1 shows a wave path from a localised near-surface defect at $\mathbf{r_s}$. In the frequency domain, the matrix of raw array data from this defect, $G_s(\omega, \mathbf{u}, \mathbf{v})$, received by the array element at $\mathbf{v}$ when the element at $\mathbf{u}$ transmits can be written in the following general form,

$$G_s(\omega, \mathbf{u}, \mathbf{v}) = \frac{A(\omega)D(\lambda, \alpha(\mathbf{u}, \mathbf{r_s}))D(\lambda, \beta(\mathbf{v}, \mathbf{r_s}))S(\omega, \alpha(\mathbf{u}, \mathbf{r_s}), \beta(\mathbf{v}, \mathbf{r_s}))\exp(ik(|\mathbf{u} - \mathbf{r_s}| + |\mathbf{v} - \mathbf{r_s}|))}{\sqrt{|\mathbf{u} - \mathbf{r_s}||\mathbf{v} - \mathbf{r_s}|}},$$

$$\tag{2}$$

where function $A(\omega)$ represents the combination of the frequency spectrum of the signal transmitted from the array controller instrument, the element impulse response functions and any frequency filtering of received data that is common to all channels. D is the directivity of an array element,[25] α and β are the incident and scattered angles at the defect with respect to the normal of the planar back wall and their values are equal to the elevation angles of the wave path of the array elements at $\mathbf{u}$ and $\mathbf{v}$ with respect to the normal of the interface between the array element and the front-wall surface. Here, only data corresponding to longitudinal wave propagation are considered and it is assumed that the only scattering processes are the reflections from the defect at $\mathbf{r_s}$.

Also shown in Figure 1 is the wave path for a specular reflection from the planar back wall of the sample occurring at position $\mathbf{r_b}$. If the sample back wall is assumed to be parallel to the array, then the corresponding expression for the first back-wall echo is,

$$G_b(\omega, \mathbf{u}, \mathbf{v}) = \frac{A(\omega)D^2\left(\lambda, \gamma\left(\mathbf{u}, \mathbf{v}, \mathbf{r_b}\right)\right)R\left(\gamma\left(\mathbf{u}, \mathbf{v}, \mathbf{r_b}\right)\right)\exp\left(\mathrm{i}k\left(|\mathbf{u} - \mathbf{r_b}| + |\mathbf{v} - \mathbf{r_b}|\right)\right)}{\sqrt{|\mathbf{u} - \mathbf{r_b}| + |\mathbf{v} - \mathbf{r_b}|}} \tag{3}$$

where γ is the incident angle (equal to the reflected angle) of the back-wall signal with respect to the normal of the back face and its value is equal to the elevation angles of the wave path of the array elements at $\mathbf{u}$ and $\mathbf{v}$ with respect to the normal of the interface between the array element and the front-wall surface, and R is the longitudinal–longitudinal reflection coefficient.[26] Hence, the total array data from a near-surface defect and the first back-wall reflection, $G(\omega, \mathbf{u}, \mathbf{v})$, are,

$$G(\omega, \mathbf{u}, \mathbf{v}) = G_s(\omega, \mathbf{u}, \mathbf{v}) + G_b(\omega, \mathbf{u}, \mathbf{v}). \tag{4}$$

The time-domain data, $g(t, \mathbf{u}, \mathbf{v}) = g_s(t, \mathbf{u}, \mathbf{v}) + g_b(t, \mathbf{u}, \mathbf{v})$, can then be obtained using an inverse fast Fourier transform (IFFT) to build up a full FMC data-set similar to that measured in an experiment. Note that related to the S-matrix definition in Section 2.1, g_s contains all scattered signals from a defect which includes both single scattering from the defect and multiple scattering between the defect and the back wall. g_b is the specular signal from the back wall and is unaffected by the defect.

Also, note that the back-wall signals from transmitter and receiver elements with the same relative position, $|\mathbf{u} - \mathbf{v}|$, are identical. G_b can therefore be simplified as n back-wall reference signals corresponding to the distances, $d = |\mathbf{u} - \mathbf{r_b}| + |\mathbf{v} - \mathbf{r_b}|$ by,

$$F_b(\omega, n) = \frac{A(\omega)B(n)\exp(\mathrm{i}kd(n))}{\sqrt{d(n)}}, \tag{5}$$

where $n = 1, 2, 3 \ldots N$, N is the total number of array elements, $B = D^2\left(\lambda, \gamma\left(\mathbf{u}, \mathbf{v}, \mathbf{r_b}\right)\right)R\left(\gamma\left(\mathbf{u}, \mathbf{v}, \mathbf{r_b}\right)\right)$. The values of d are ordered in $|\mathbf{u} - \mathbf{v}|$, i.e. $|\mathbf{u} - \mathbf{v}| = 0, p, \ldots, (n-1)p, \ldots, (N-1)p$, where p is the pitch distance of array elements. As before, the time-domain back-wall reference signal, $f_b(t, n)$, can then be obtained using an IFFT.

3. S-matrix extraction for a near-surface defect

Here, the TFM imaging algorithm [14] was used as an example of an ultrasonic array imaging algorithm. In the TFM, each image pixel value can be written as a weighted sum of
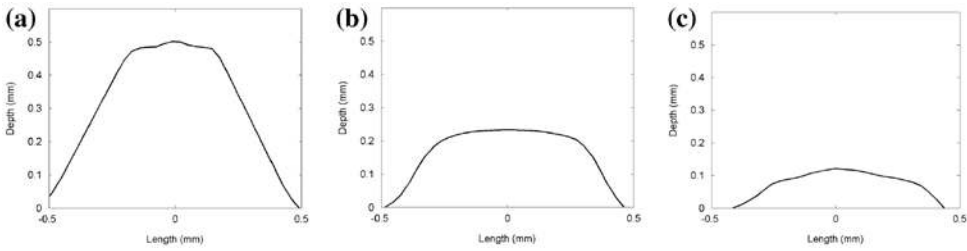
Figure 2. Surface profiles of defects in sample #1 measured using a stylus profilometer where figure parts (a)–(c) correspond to defects #1–3, respectively.

Table 1. Specification of the array transducer used in simulation and experimental measurements.

Number of element, N	Central frequency (MHz)	Element width (mm)	Element pitch, p (mm)	Array aperture size (mm)
64	15	0.20	0.21	13.23

contributions from certain points at the time of each time-domain signal from the data acquired by the array. Mathematically, the intensity of the pixel at position, $\mathbf{p}$, can be written as,

$$I(\mathbf{p}) = \left| \sum_{\mathbf{u}} \sum_{\mathbf{v}} g(\tau(\mathbf{u}, \mathbf{v}, \mathbf{p}), \mathbf{u}, \mathbf{v}) \right|, \tag{6}$$

where $\tau(\mathbf{u}, \mathbf{v}, \mathbf{p})$ is the travelling time for a wave emitted from an element at $\mathbf{u}$ to a pixel at $\mathbf{p}$ and back to an element at $\mathbf{v}$ and is commonly referred to as a delay law. Once the defect has been located in the TFM image, the S-matrix can be extracted if the scattered signals from the defect can be separated from the back-wall signals in the FMC data-set. Often, in the FMC data-set, the signals scattered from the defect and those reflected from the back-wall overlap in both time and frequency domains and this makes the defect S-matrix extraction difficult.

In this section, the defect/back-wall signal overlap problem is explored using simulated FMC data from a 7-mm-thick aluminium plate with a rounded notch located on the back wall. In the FMC data simulation, the surface profile of the modelled near-surface defect used an experimentally measured notch profile. This profile was measured using a stylus profilometer (Talysurf, Taylor Hobson, Leicester, UK) and is shown in Figure 2. As shown in Figure 2, the widths of these defects are around 2.3λ and heights are 1.1λ, 0.5λ and 0.2λ for defects #1–3, respectively. An ultrasonic array specified in Table 1 was simulated (and later explored experimentally) and was placed on the top surface of the plate with its centre aligned to the near-surface defect to achieve largest angular inspection coverage. A longitudinal wave speed for aluminium of $c = 6400$ m/s was used in the simulation. Figure 3 shows a flow chart of how to extract the S-matrix of a near-surface defect from the FMC data-set. This includes FMC data categorisation and defect signal extraction which are discussed in the next section.

3.1. FMC data categorisation

Figure 4 shows a TFM image of the simulated defect, in which the defect can be identified around the back wall. Once the location of the defect and back wall is found from the images
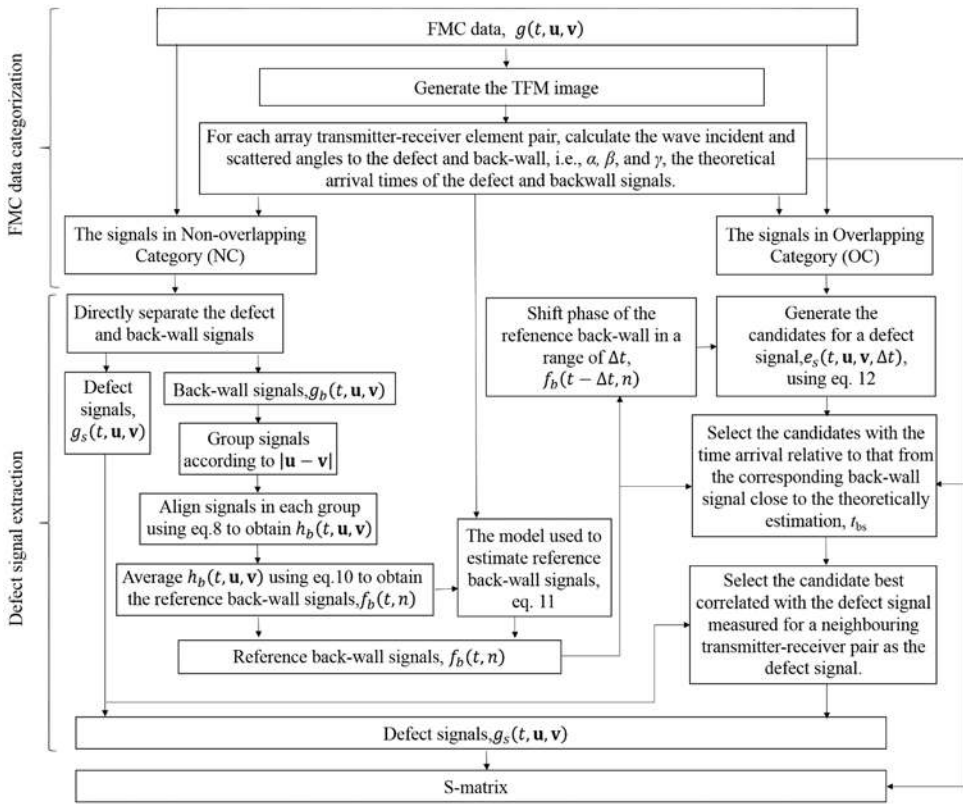
Figure 3. Flow chart of the near-surface defect S-matrix extraction.
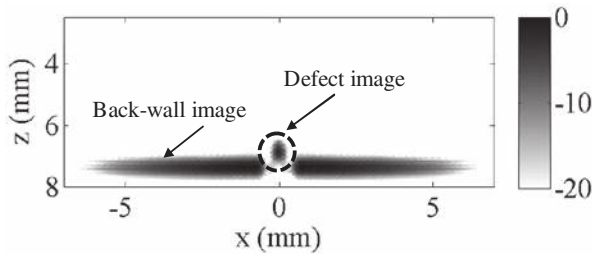
Figure 4. TFM image from the simulated FMC data for the structure shown in Figure 1.

in Figure 4, the incident and scattered angles at the defect, i.e. α and β, as well as the theoretical arrival times of the defect and back-wall signals can be calculated. Figure 5 compares two typical time-domain signals obtained from the simulated FMC data which highlight the overlap problem. Figure 5(a) shows the signal when the left-most array element acts as both a transmitter and a receiver. In this case, the signal scattered from the defect can be directly extracted from the overall signal due to the large separation time t_{bs},

$$t_{bs}(\mathbf{u}, \mathbf{v}) = \frac{\left(|\mathbf{u} - \mathbf{r_s}| + |\mathbf{v} - \mathbf{r_s}|\right) - \left(|\mathbf{u} - \mathbf{r_b}| + |\mathbf{v} - \mathbf{r_b}|\right)}{c}, \tag{7}$$

Figure 5. Typical signals in the simulated FMC data-set to highlight the overlap problem when (a) the left-most array element acts as both a transmitter and a receiver and (b) the middle array element acts as both a transmitter and a receiver.
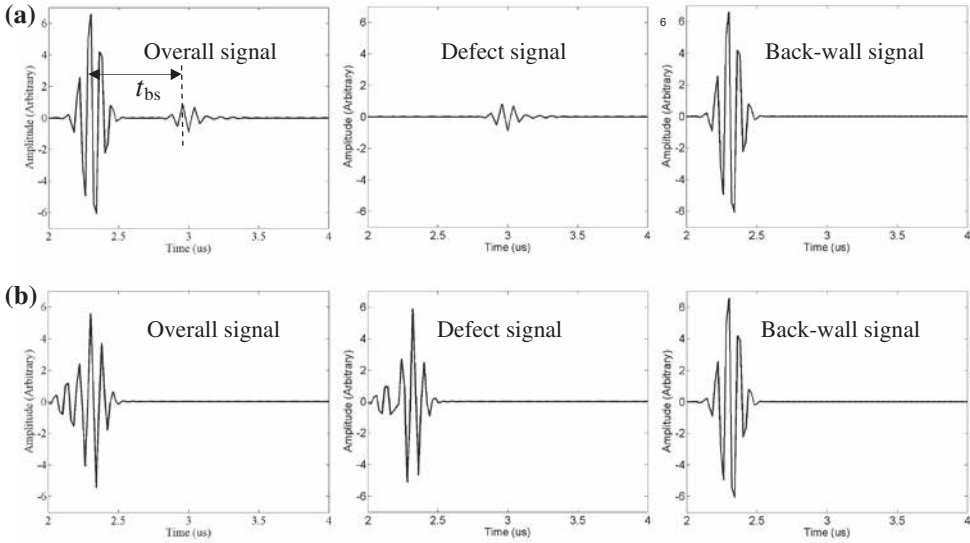
where $|\mathbf{u} - \mathbf{r_s}|, |\mathbf{v} - \mathbf{r_s}|, |\mathbf{u} - \mathbf{r_b}|$ and $|\mathbf{v} - \mathbf{r_b}|$ can be approximately measured from the TFM image of the structure. Figure 5(b) shows the case in which the middle array element acts as both a transmitter and a receiver. In this case, the signal scattered from the defect overlaps with that from the back wall and cannot be directly separated based on the time of arrival alone. Note that the arrival time of a defect signal depends on both its location and size. Here, it is assumed that a defect is small, its size less than two wavelengths, and hence, the location difference between the defect and the specular reflection point on the back wall dominates the arrival time difference between the defect and the back-wall signals.

Using a threshold for t_{bs}, e.g. the width of the transmitted signal, the signals in the FMC data can be classified into two categories. The signals in the non-overlapping category (NC) have t_{bs} longer than the threshold and those in the overlapping category (OC) have t_{bs} shorter than the threshold. Figure 6 shows these two categories for the simulated FMC signals, from which it can be seen that the majority of signals fall into the OC.

3.2. Defect signal extraction

3.2.1. Extraction of reference back-wall signals from non-overlapping signals

As shown in the left-hand part of the flow chart shown in Figure 3, if the defect and back-wall signals, i.e. $g_s(t, \mathbf{u}, \mathbf{v})$ and $g_b(t, \mathbf{u}, \mathbf{v})$, fall into the NC, then they can be directly separated from the overall signals, i.e. $g(t, \mathbf{u}, \mathbf{v})$. The separated back-wall signals are then grouped according to $|\mathbf{u} - \mathbf{v}|$. To reduce the effect of random element phase errors in experimental measurements, in each group n, the back-wall signals are phase shifted to align with a reference signal chosen from within the group,

$$h_b(t, \mathbf{u}, \mathbf{v}) = g_b\big(t - \Delta t_b, \mathbf{u}, \mathbf{v}\big) \tag{8}$$
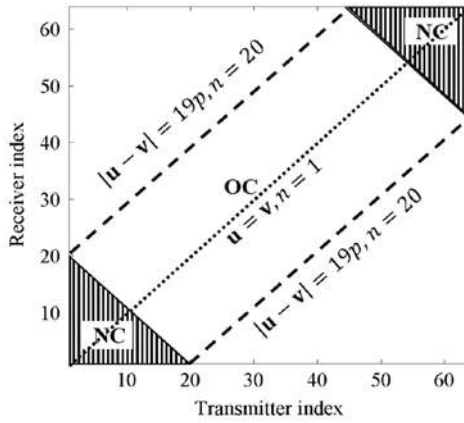
Figure 6. Overlapping and non-overlapping categories in the simulated FMC data based on the array described in Table 1 and geometry shown in Figure 1.

where Δt_b is the time shift measured by the cross correlation between $g_b(t - t, \mathbf{u}, \mathbf{v})$ and the reference signal, $q_b(t, n)$,

$$\Delta t_b = \underset{\Delta t}{\operatorname{argmax}} \left(g_b(t - \Delta t, \mathbf{u}, \mathbf{v}) \times q_b(t, n) \right), \tag{9}$$

where the operator argmax is to find Δt which leads to the maximum value of the defined function and $q_b(t, n)$ is the signal from the transmitter–receiver pair with minimum $|\mathbf{u} + \mathbf{v}|$ in group n.

The aligned signals within each group $h_b(t, \mathbf{u}, \mathbf{v})$ are then averaged and stored as candidate back-wall reference signals,

$$f_b(t, n) = \langle h_b(t, \mathbf{u}, \mathbf{v}) \rangle, \tag{10}$$

where $\langle \quad \rangle$ denotes average and is taken for all measured h_b within a group with the same $|\mathbf{u} - \mathbf{v}|$.

Note that the purpose of equation eight is to align the measured back-wall signals. $q_b(t, n)$ can be from any transmitter–receiver pair in group n and this will not affect the S-matrix extraction because $f_b(t, n)$ will be phase shifted over a small time range to extract a defect signal in Equation (12). Here, choosing the signal from the transmitter–receiver pair with minimum $|\mathbf{u} + \mathbf{v}|$ in group n as $q_b(t, n)$ is only for defining a simple process.

Note that the number of back-wall reference signals that can be extracted using Equations (8–10) depends on how many $|\mathbf{u} - \mathbf{v}|$ signals fall into the NC. The FMC data corresponding to transmitter–receiver indices of the signals with the same $|\mathbf{u} - \mathbf{v}|$ are distributed along the diagonal lines shown in Figure 6. For example, there are 20 available signals in the NC which can be used to calculate $f_b(t, 1)$; however, no signals can be used to calculate $f_b(t, n \geq 20)$.

3.2.2. Propagation of non-overlapping signals to create reference back-wall signals for overlapping cases

The signals reflected from the back wall with large incident angles overlap with defect signals and cannot be directly extracted from the FMC data. Instead, using Equation (5),

such back-wall reference signals can be simulated by propagating extracted non-overlapping signals as,

$$F_b(\omega, n) = F_b(\omega, n - 1) \frac{B(n)\exp(ikd(n)) \sqrt{d(n-1)}}{B(n-1)\exp(ikd(n-1)) \sqrt{d(n)}}, \tag{11}$$

where B and d can be calculated from the defect and back-wall locations in the TFM image. The approach proceeds by the sequential application of Equation (11) to estimate the remaining back-wall reference signals. In the example discussed, this process starts when the FMC data-set $f_b(t, 20)$ is used in Equation (11) to estimate $f_b(t, 20)$ and hence $f_b(t, n > 20)$ is then sequentially estimated to form a complete set of back-wall reference signals.

3.2.3. Extraction of defect signals by subtraction

As shown in the right-hand part of the flow chart in Figure 3 for OC signals, the defect signals, $g_s(t, \mathbf{u}, \mathbf{v})$, can be extracted by the subtraction of suitable back-wall reference signals, $f_b(t, n)$, from the overall signals, $g(t, \mathbf{u}, \mathbf{v})$. In an effort to reduce phase errors which lead to signal misalignment and hence subtraction errors, the reference back-wall signals are first phase shifted over a small range, Δt, and then used for subtraction to generate a group of decomposed signals by,

$$e_s(t, \mathbf{u}, \mathbf{v}, t) = g(t, \mathbf{u}, \mathbf{v}) - f_b(t - \Delta t, n), \tag{12}$$

Note that these phase-shifted subtracted signals, e_s, are all possible candidates for the defect signal. To select the best matched candidate, first, the signals with an arrival time relative to the back-wall signal, $f_b(t - \Delta t, n)$, close to the theoretical estimation, t_{bs}, are selected (within a tolerance difference of 0.017 μs which corresponds to the wave-travelling distance of $\lambda/4$). Note that this difference threshold is based on the simulation works and it is assumed that the signal noise level is low and would not affect on phase calculation. Secondly, the cross correlation coefficients between these selected candidates and the defect signal previously measured for a neighbouring transmitter–receiver pair are calculated. It is known that the S-matrix of a defect in the angular range of the inspection is continuous,[16,24] hence the defect signals from neighbouring transmitter–receiver pair are highly correlated. The candidate resulting in the highest correlation coefficient is hence chosen as the defect signal. The measured defect signals are finally used to generate the S-matrix of the defect.

In summary, and with reference to the flowchart shown in Figure 3, the procedure of the S-matrix extraction for a near-surface defect based on the FMC data-set is

(1) identify the defect and back wall in a TFM image;
(2) calculate the arrival time, incident and scattered angles from each transmitter–receiver element pair to the defect and back wall;
(3) categorise signals in the FMC into NC and OC. This is based on the arrival time difference between the signals from the defect and the back wall for each combination of transmitter and receiver array elements;
(4) directly extract the defect and back-wall signals from the signals in the NC;
(5) calculate the full set of back-wall reference signals, $f_b(t, n)$, using Equations (8–11);
(6) generate the defect signal candidates, $e_s(t, \mathbf{u}, \mathbf{v}, \Delta t)$, for the signals in the OC using Equation (12). Measure the defect signals by subtracting the reference back-wall signal following the steps below:

     (a) first, choose the signal candidates with a time arrival relative to that from the corresponding back-wall signal close to the theoretical estimation, t_{bs};

     (b) second, select the signal candidate best correlated with the defect signal measured for the neighbouring transmitter–receiver pair as the defect signal;

   7. generate a scattering matrix using the measured defect signals, $g_s(t, \mathbf{u}, \mathbf{v})$.

4. Results

The performance of the proposed defect S-matrix measurement method is assessed through a comparison of the experimentally measured and simulated S-matrices from the notch defects on the back wall of the sample shown in Figure 2. The main measurement errors are also analysed in this section.

4.1. Experimental set-up

Figure 2(a)–(c) shows surface profiles of the surface defects 1–3 which were made in a 7-mm-thick aluminium block, sample #1. Another sample #2 with the same geometry as sample #1 but without defects was also made and used to investigate the error sources associated with the S-matrix extraction process described in Section 3.2. In the experimental measurements, the array is placed on the top surface of the sample and its centre is aligned in turn with the centre of each defect. Note that the experimental S-matrix extraction presented in Sections 4.2 and 4.3 used a single FMC data-set for each defect.

    A 15-MHz linear array with 64 elements (manufactured by Imasonic, Besancon, France), of parameters shown in Table 1, was used in the experiments. A commercial array controller (Micropulse MP5PA, Peak NDT, Ltd., Derby, UK) was used to capture the complete set of time-domain signals from every transmitter–receiver pair of the ultrasonic array (i.e. the FMC data-set). The captured data were then exported and processed using MATLAB (The MathWorks, Inc., Natick, MA). Note that the captured FMC data-sets contain the raw time-domain signals. Coupling gel (Sonagel-W250, Sonatest Ltd., Milton Keynes, UK) was used to couple the array probe and a specimen. In the experimental measurements, the array probe was held by a hand as it is used in practice.

4.2. Experimentally measured TFM images and back-wall signals

Figure 7(a)–(c) shows images from defects 1–3 using the TFM imaging algorithm [14], when the array is located centrally over each defect. Note that the accurate probe positioning was achieved by observing the real-time TFM image to make sure that the defect image centre is at $x = 0$ mm. Also note that the TFM images in Figure 7 are only plotted in the image region, 3 mm $\leq z \leq$ 8 mm, and the amplitude region from −20 to 0 dB. The images in the other regions will not affect the S-matrix extraction and hence are not plotted. These images show the location of the defect; however, the defect image is mixed with the back-wall image and cannot be directly isolated from the overall image. Figure 8 compares the peak amplitude of the back-wall reference signals from the simulation with that from experimental measurements on samples #1 and #2. Note that there are three curves measured from sample #1 when the array was sequentially aligned with defects 1–3 and these curves are plotted
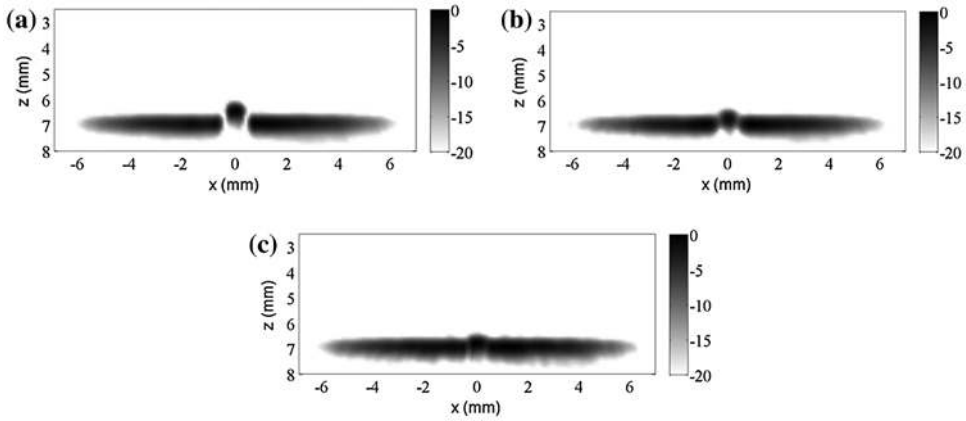
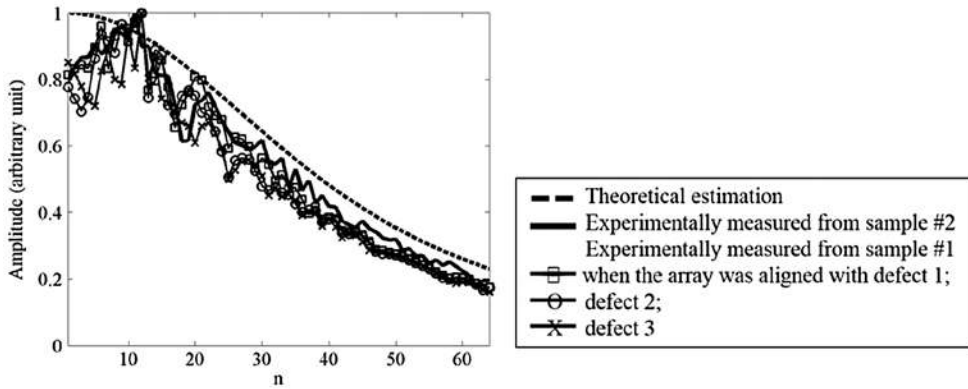**Figure 7.** TFM images for a near-surface defect with a surface profile as shown in Figure 2((a)–(c)).

Figure 8. Comparison of the peak amplitude of the back-wall reference signals from theoretical estimation (dashed curve) and experimental measurement from samples #1 (three curves with square, circle and cross symbols) and #2 (solid curve).

with square, circle and cross symbols, respectively. The good agreement between the experimental measurements on samples #1 and #2 demonstrates the robustness of the back-wall reference signal measurement. In addition, the good agreement between the simulated and experimental measurements validates the forward model for back-wall signal estimation. Note that the difference between the simulated and experimental measurements is mainly caused by the coupling inconsistency between each array element and the top surface of a specimen and this will be further discussed in Section 4.4.

4.3. S-matrix comparison

The physical meaning of the S-matrix and how to calculate it theoretically are described in Section 2.1. Note that the shape of the S-matrix for a smooth crack is unique as a function of crack size divided by wavelength, the incident and scattered angles at the defect, i.e. α and β defined in Figure 1, and hence can be used to classify and size the crack without
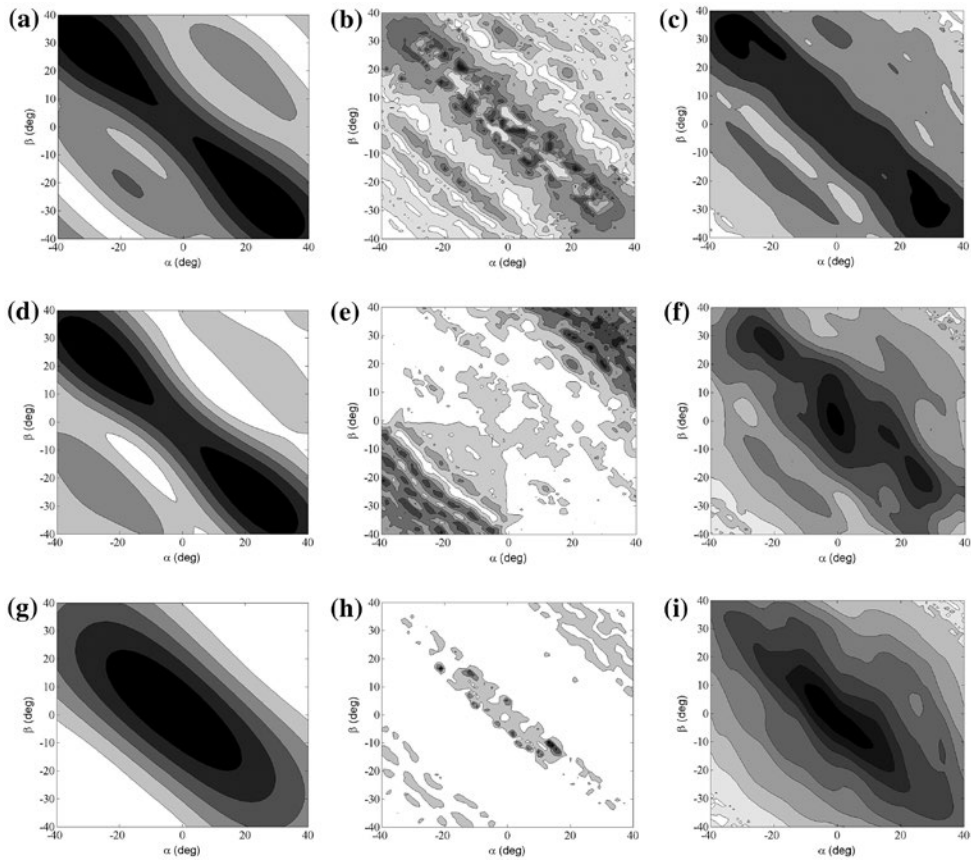
Figure 9. Comparison of S-matrices obtained from ((a), (d), (g)) an FE model, the experimentally measured FMC data-set ((b), (e), (h)) without and ((c), (f), (i)) with the subraction process. ((a)–(c)), ((d)–(f)) and ((g)–(i)) are from defects 1–3 in sample #1, respectively.
Note: In each figure, the amplitude is normalised to its own maximum with a linear scale.

measuring scattering amplitude.[11,12,15,16] Note that the location of the defect and back wall in Figure 7 can be identified and used to calculate α and β, as described in Section 3.1.

The performance of the proposed S-matrix extraction method was assessed through the comparison of the measured and simulated S-matrix from the notch defects on the back wall of sample #1. Figure 9((a), (d), (g)) shows the simulated S-matrices for defects 1–3, respectively. Note that the amplitude is normalised to its own maximum with a linear scale in each figure and hence only S-matrix shape is compared. Also note that the non-symmetry of each simulated S-matrix is caused by the non-symmetrical surface profiles of the corresponding simulated defect (which were extracted from the experimentally measured surface profiles shown in Figure 2). Figure 9((b), (e), (h)) shows the experimentally measured S-matrices extracted directly using Equation (2) for the FMC data-set. Figure 9((c), (f), (i)) shows the experimentally measured S-matrices extracted using the subtraction process outlined in Figure 3. The results in Figure 9((b), (e), (h)) and ((c), (f), (i)) can then be compared with the predicted S-matrices in Figure 9((a), (d), (g)) and this is indicated by the correlation coefficient between them. The measured correlation coefficients between the simulated and

Table 2. Measured correlation coefficients between the simulated and experimentally measured S-matrices.

Defect #	1	2	3	1	2	3
Simulated S-matrix	Figure 9(a)	Figure 9(d)	Figure 9(g)	Figure 9(a)	Figure 9(d)	Figure 9(g)
Experimentally measured S-matrix	Figure 9(b)	Figure 9(e)	Figure 9(h)	Figure 9(c)	Figure 9(f)	Figure 9(i)
Correlation coefficient	0.73	−0.40	−0.11	0.91	0.84	0.93
S-matrix extraction method	Without the subtraction process			With the subtraction process		

experimentally measured S-matrices of each defect are listed in Table 2. From Table 2, it can be seen that the improved measurement, indicated by the higher correlation coefficients, is achieved using the proposed method with the subtraction process. This also indicates that when the database of the S-matrix of near-surface defects is built up, the proposed method has the potential to help to classify and size the near surface-breaking cracks by searching the best matched shape in the S-matrix database which is similar to the methods used for classifying and sizing smooth cracks.[11,12,15–17]

4.4. Discussion of errors

In the proposed S-matrix extraction method using the subtraction process, one main error source is from the back-wall signal measurement. Here, the experimental back-wall measurements from sample #2 are used to investigate the S-matrix extraction measurement error sources. There is no defect in sample #2 and hence the signals reflected from the back wall from each transmitter–receiver pair can be extracted easily from the FMC data-set. In order to investigate the back-wall measurement error, a 1-mm (>2λ)-wide observation region on the back wall directly below the array centre is used. Note that the size of this observation region is approximately the same as the size of the notch on the back wall of sample #1. The signals reflected from the back wall with a reflected point within the observation region were labelled as 'true' signals and the averaged signals from other reflected signals from the back wall with the same incident angle were labelled as the 'measured' signals. Note that, for each incident angle, there is only one 'measured' signal but could be several 'true' signals from different transmitter–receiver element pairs.

Figure 10(a) compares the range of the true signals (i.e. both the min and max are plotted) with the averaged measured signals for each incident angle, γ. The peak amplitude difference between the true and measured values is used as a measurement error metric, i.e.

$$\text{Error} = 20 \log \left| \frac{\text{measured value - true value}}{\text{true value}} \right|, \qquad (13)$$

and is shown in Figure 10(b). Note that the peak amplitude is not from a rectified signal but a raw time-domain signal in a FMC array data-set. From this figure, it can be seen that the mean errors across a range of incident angles vary from −30 to −12 dB. The significance of these errors for the extracted S-matrices will depend on the amplitude of the signal from the defect itself. For example, if the amplitudes of the scattered defect signals are comparable to those from the back wall, then these errors will translate directly into errors in the process of defect extraction by subtraction described in Section 3.2.3.

The measurement error due to inconsistent coupling of the array to the structure is further analysed by repeating the above procedure 100 times on sample #2. In each case,
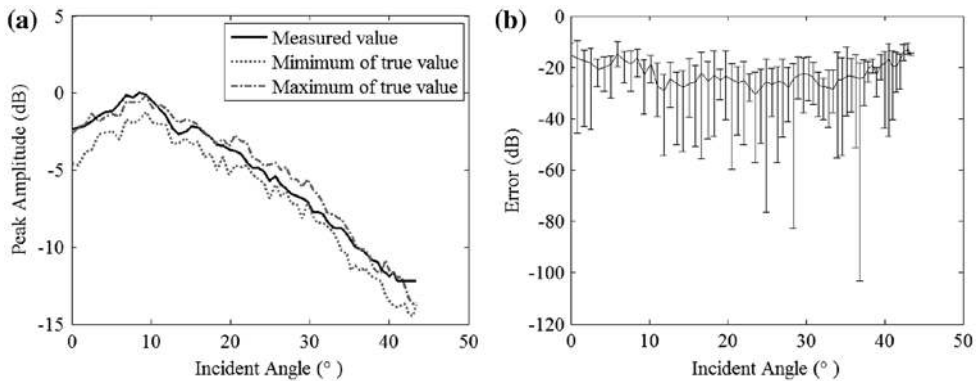
Figure 10. Experimental results of the peak amplitude of the back-wall signals from sample #2 (a) the comparison of the averaged measured value with the maximum and minimum true values and (b) the measurement error.
Note: The amplitudes are normalised to the maximum value over all amplitudes.
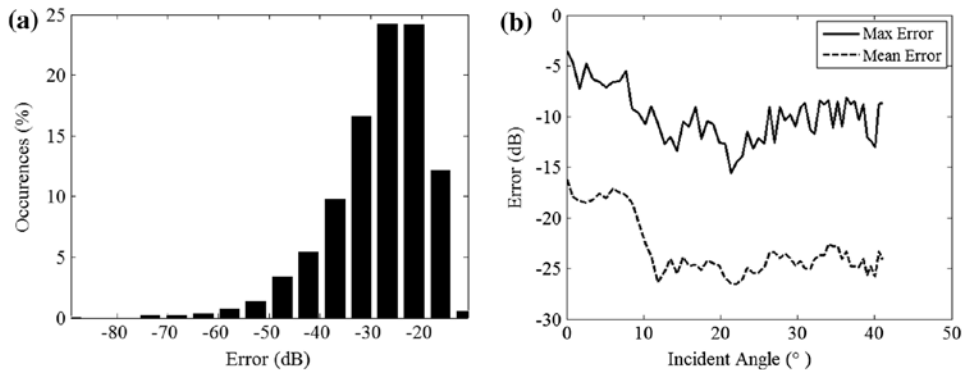

Figure 11. Experimental results of the peak amplitude of the back-wall signals from 100 repeated measurements on sample #2 for (a) the occurrence of the error at $\Gamma = 16°$ and (b) the errors as a function of incident angle.

the array probe was removed, re-placed and re-coupled in the same position. The accuracy of the re-positioning was achieved by a mechanical holder placed above the sample. Figure 11(a) shows the measurement error distribution at $\gamma = 16°$ and this shows a mode error of around −25 dB. Figure 11(b) shows the maximum and average errors for all incident angles based on 100 measurements. From Figure 11(b), the mean error is seen to vary between −16 and −26 dB, which is similar to the errors shown in Figure 10 suggesting that coupling inconsistency is the dominant source of error and can significantly distort the measured back-wall signals and the shape of a measured S-matrix. It is also shown that the maximum error (i.e. the worst case scenario) varies between −5 dB for the case of $\gamma = 0°–8°$ and around −10 dB for most other angle cases. Note that the occurrence of the worst-case scenario is less than 1% and should be rarely happened in the experimental measurement. This analysis suggests that the S-matrix extraction process could be further improved if coupling inconsistency could be minimised, for example, by performing the experiments in immersion.

5. Conclusion

A method was developed to extract scattered signals from a near-surface defect from within the FMC data-set. This involved separating defect signals from the back-wall signals. In the process, the signals in the FMC data-set were first divided into NC and OC. The reference back-wall signals were then measured using the separable back-wall signals from the NC. Firstly, the defect signals were directly extracted from the overall signals in the NC. Secondly, the defect signals in the OC were extracted by subtraction of the overall signals from the measured reference back-wall signals. The extracted scattered signals from a near-surface defect were then used to measure its S-matrix. An experimental validation was performed on a sample with three machined notches and the measured S-matrices showed a generally good agreement with the corresponding predictions using an FE model. The measurement error was quantitatively investigated using the FMC data-set from a sample without a defect. It was shown that the average measurement error of the peak amplitude of the signals reflected from the back wall ranges from −26 to −16 dB and this was mainly due to an inconsistent coupling layer across the array. This leads to errors in the above subtraction process resulting in residual errors in the extracted S-matrix. It is noted that one assumption in the paper is that the defect is detectable and hence the defect location is known. In this case, in order to increase measurement accuracy, the array should be aligned with the defect as much as possible to reduce back-wall reference measurement error. However, if the array is not possible to be aligned with the defect, the proposed method should still work but with more measured back-wall reference signals from the model, which is used to estimate the reference signals from the OC. The proposed work contributes to classification and characterisation of surface defects.

Acknowledgements

ORCID

Jie Zhang 🆔 http://orcid.org/0000-0001-7886-5053

References

[1] Collins JA. Failure of materials in mechanical design: analysis, prediction, prevention. New York [NY]: Wiley; 1993.

[2] William CD. Materials science and engineering—an introduction. New York [NY]: Wiley; 1997.

[3] Hesse D, Cawley P. A single probe spatial averaging technique for guided waves and its application to surface wave rail inspection. IEEE Trans. Ultrason. Ferroelectr. Freq. Control. 2007;54:2344–2356.

[4] Edwards RS, Sophian A, Dixon S, et al. Dual EMAT and PEC non-contact probe: applications to defect testing. NDT & E Int. 2006;39:45–52.

[5] Edwards RS, Dixon S, Jian X. Depth gauging of defects using low frequency wideband Rayleigh waves. Ultrasonics. 2006;44:93–98.

[6] Rokhlin SI, Kim JY. In situ ultrasonic monitoring of surface fatigue crack initiation and growth from surface cavity. Int. J. Fatigue. 2003;25:41–49.

[7] Rose JL, Avioli MJ, Mudge P, et al. Guided wave inspection potential of defects in rail. NDT & E Int. 2004;37:153–161.

[8] Coccia S, Bartoli I, Marzani A, et al. Numerical and experimental study of guided waves for detection of defects in the rail head. NDT and E Int. 2011;44:93–100.

[9] Satyarnarayan L, Pukazhendhi DM, Balasubramaniam K, et al. Phased array ultrasonic measurement of fatigue crack growth profiles in stainless steel pipes. J. Pressure Vessel Technol. Trans. ASME. 2007;129:737–743.

[10] Prager J, Kitze J, Acheroy C, et al. SAFT and TOFD—a comparative study of two defect sizing techniques on a reactor pressure vessel mock-up. J. Nondestr. Eval. 2013;32:1–13.

[11] Velichko A, Wilcox PD. Efficient finite element modelling of elastodynamic scattering from near surface and surface breaking defects. In: Thompson DO, Chimenti DE, editors. Review of progress in QNDE, 30. Melville, NY: American Institute of Physics; 2010. p. 59–66.

[12] Velichko A, Wilcox PD. Detection of near-surface and surface-breaking defects using ultrasonic arrays. In: Thompson DO, Chimenti DE, editors. Review of progress in QNDE, 32. Melville, NY: American Institute of Physics; 2012. p. 929–936.

[13] Felice MV, Velichko A, Wilcox PD. Accurate depth measurement of small surface-breaking cracks using an ultrasonic array post-processing technique. NDT and E Int. 2014;68:105–112.

[14] Holmes C, Drinkwater BW, Wilcox PD. Post-processing of the full matrix of ultrasonic transmit-receive array data for non-destructive evaluation. NDT and E Int. 2005;38:701–711.

[15] Zhang J, Drinkwater B, Wilcox P. The use of ultrasonic arrays to characterize crack-like defects. J. Nondestr. Eval. 2010;29:222–232.

[16] Zhang J, Drinkwater B, Wilcox P. Defect characterization using an ultrasonic array to measure the scattering coefficient matrix. IEEE Trans. Ultrason. Ferroelectr. Freq. Control. 2008;55:2254–2265.

[17] Bai L, Velichko A, Drinkwater B. Ultrasonic characterization of crack-like defects using scattering matrix similarity metrics. IEEE Trans. Ultrason. Ferroelectr. Freq. Control. 2015;62:545–559.

[18] Zhang J, Drinkwater B, Wilcox P. Longitudinal wave scattering from rough crack-like defects. IEEE Trans. Ultrason. Ferroelectr. Freq. Control. 2011;58:2163–2171.

[19] Zhang J, Drinkwater B, Wilcox P. Effect of roughness on imaging and sizing rough crack-like defect using ultrasonic arrays. IEEE Trans. Ultrason. Ferroelectr. Freq. Control. 2012;59:939–948.

[20] Schmerr LW. Fundamentals of ultrasonic nondestructive evaluation – a modeling approach. New York, NY: Prenum Press; 1998.

[21] Zhang J, Drinkwater BW, Wilcox PD, et al. Defect detection using ultrasonic arrays: the multi-mode total focusing method. NDT and E Int. 2010;43:123–133.

[22] Lopez-Sanchez AL, Kim H, Schmerr LW Jr. Measurement models and scattering models for predicting the ultrasonic pulse-echo response from side-drilled holes. J. Nondestr. Eval. 2005;24:83–96.

[23] Ogilvy JA. Theory of wave scattering from random rough surfaces. Bristol: Adam Hilger; 1991.

[24] Velichko A, Wilcox P. A generalized approach for efficient finite element modelling of elastodynamic scattering in two and three dimensions. J. Acoust. Soc. Am. 2010;128:1004–1014.

[25] Miller FG, Pursey H. The field and radiation impedance of mechanical radiators on the free surface of a semi-infinite isotropic solid. Proc. R. Soc. London. 1954;34:521–541.

[26] Krautkramer J, Krautkramer H. Ultrasoinc testing of materials. New York, NY: Springer Verlag; 2003.